


# UV-assisted synthesis of reduced graphene oxide–ZnO nanorod composites immobilized on Zn foil with enhanced photocatalytic performance

Sina Abdolhosseinzadeh<sup>1</sup> · Hamed Asgharzadeh<sup>1</sup>  · Sina Sadighikia<sup>2</sup> · Alireza Khataee<sup>3</sup>

Received: 9 June 2015 / Accepted: 21 September 2015 / Published online: 8 October 2015  
© Springer Science+Business Media Dordrecht 2015

**Abstract** ZnO nanorods were hydrothermally grown on Zn foil in an alkaline solution and the immobilized nanorods were subsequently hybridized with reduced graphene oxide (rGO) through UV-assisted photocatalytic reduction of graphene oxide (GO). X-ray diffraction analysis confirmed the vertical growth of ZnO nanorods while the incorporation of rGO to ZnO was investigated by scanning electron microscopy and photoluminescence spectroscopy. The successful photocatalytic reduction of GO was demonstrated by means of Raman spectroscopy and X-ray photoelectron spectroscopy. The photocatalytic behavior and photostability of the sandwich-like rGO–ZnO composite were studied through decolorization of the aqueous solution of acid orange 7 under UV-C illumination. The rGO–ZnO photocatalyst presented higher dye decomposition efficiency than pure ZnO. The hybridization of rGO and ZnO led to a 40 % increase in the pseudo-first-order kinetic model's rate constant and an enhancement of the photostability. The role of incorporation of rGO in enhancement of the ZnO's photostability has been elucidated in the light of specific features of the sandwich-like architecture.

**Keywords** ZnO nanorods · Nanocatalyst · Graphene · Photocatalysis · Photocorrosion

---

✉ Hamed Asgharzadeh  
asgharzadeh@tabrizu.ac.ir

<sup>1</sup> Department of Materials Engineering, University of Tabriz, Tabriz 51666-16471, Iran

<sup>2</sup> Faculty of Engineering and Natural Sciences, Sabanci University Nanotechnology Research and Application Center, Orhanli-Tuzla, 34956 Istanbul, Turkey

<sup>3</sup> Research Laboratory of Advanced Water and Wastewater Treatment Processes, Department of Applied Chemistry, Faculty of Chemistry, University of Tabriz, Tabriz 51666-16471, Iran

## Introduction

Over the last decades, the rapidly increasing production of hazardous wastes as an undesirable consequence of industrial development has become a serious challenge. Photocatalysis is extensively employed for the decontamination of pollutants mainly due to its effectiveness and easy operation [1]. Nevertheless, its efficiency is far lower than the expectations for an economically justifiable process. The major drawbacks that drastically degrade the photocatalytic behavior are the low quantum efficiency and in some cases the photocorrosion of the most of photocatalyst materials [2, 3]. Among the different strategies proposed for addressing each of these limitations, the compositing with carbonaceous nanomaterials such as nanotubes [4], fullerenes [5], and graphenes [6] is of greater interest due to their effective and simultaneous contribution in resolving both of the aforementioned issues. Graphene, a single layer of  $sp^2$ -bonded carbon atoms with many outstanding properties like high surface area and high electron conductivity and mobility [7], has stimulated enormous scientific interest and a great number of investigations have been devoted to study its role in the enhancement of photocatalytic activity of semiconductors [8]. It has been shown that the synergetic effect between CdS and reduced graphene oxide (rGO) directly influences the charge-transport property and band-structure of the composite [9]. The rapid charge transfer from semiconductor to graphene effectively prolongs the electron-hole separation, resulting in an increased photocatalytic activity [10]. Similar synergistic effects in composites of graphene with other semiconductor materials have been frequently reported [11–13]. Furthermore, it has been stated that the incorporation of graphene to some photocatalyst materials susceptible to photocorrosion (such as ZnO and CdS), results in a significant enhancement of their photostability [14, 15].

ZnO with a direct wide band gap ( $\sim 3.37$  eV), large excitation binding energy ( $\sim 60$  meV), high photosensitivity, and low cost is a well-known photocatalyst material [16]. Photocatalytic degradation of water contaminations by means of nanostructured ZnO is a promising approach for treatment of waste water [17]. Owing to the diverse growth systems in ZnO, numerous morphologies in nanoscale are attainable by tailoring the growth variables [18]. Investigation of the photocatalytic activity of various morphologies of ZnO indicates that 1D nanostructures such as nanorods and nanowires are more efficient than their zero and two-dimensional counterparts [19, 20]. 1D ZnO nanostructures can be synthesized by both gas-phase deposition methods (e.g., thermal evaporation, chemical vapor deposition, and laser ablation) and liquid-phase approaches (e.g., hydrothermal/solvothermal, liquid phase deposition, and electrochemical growth) [21–25]. Nonetheless, liquid-phase techniques are highly preferred due to their relative simplicity, cost-effectiveness, and lower processing temperature [26]. Unfortunately, ZnO suffers from both low quantum efficiency and photocorrosion and its hybridization with graphene can be employed for resolving these problems. In order to hybridize the ZnO nanostructures with graphene or rGO, several methods have been developed, which can be classified into three main categories: (1) Reduction of graphene oxide (GO) on ZnO [27–29]; (2) Growth of ZnO on rGO

[30–33]; (3) Simultaneous synthesis of ZnO and reduction of GO [1, 6, 34]. The overall process and specifically the morphology tailoring is much easier through the first approach in which the reduction of GO is usually carried out by means of chemical reducing agents like hydrazine [27]. Nevertheless, a hazardous reducing agent is generally required in this technique and the prepared composite may suffer from improper connection between ZnO and rGO. The photocatalytic reduction of GO on ZnO is a room-temperature and environmentally friendly protocol that ensures an efficient interaction between composite components, especially in the case of immobilized nanostructures. In this process, the reduction of GO and subsequent attachment of rGO to ZnO occurs simultaneously through the transfer of photogenerated electrons from ZnO to GO, while the remaining holes are consumed by a hole-scavenger agent (e.g., ethanol) [35]. Recently, rGO platelets hybridized by ZnO nanoparticles have been successfully synthesized via UV-assisted photocatalytic reduction [28, 35, 36].

Regardless of the compositing method, the application of photocatalysts in the form of nanopowders necessitates several post-treatments for separation of the photocatalyst from the treated water, which limits their industrial applications. Immobilization of the nanostructured photocatalysts on suitable substrates prevents from their agglomeration and facilitates their separation from the processed water [37, 38]. Nevertheless, to the best of our knowledge, the hybridization of rGO with immobilized ZnO nanorods and their photocatalytic behavior have not been reported yet. Herein, firstly we grew vertically aligned ZnO nanorods on a Zn substrate via a simple hydrothermal method. It is worthy to note that hydrothermal growth in alkaline solutions containing  $\text{Zn}^{2+}$  ions is the most widely used liquid-phase method for synthesis of ZnO nanostructures [39]. Then, the synthesized nanoarrays were coated with rGO by means of UV-assisted reduction to enhance the photocatalytic activity and to protect ZnO from photocorrosion. The photocatalytic activity of the rGO–ZnO was evaluated through degradation of acid orange 7 (AO7) under UV light illumination. The characteristics of rGO–ZnO composite are presented and its photocatalytic performance is compared with pure ZnO. Moreover, the kinetics of the photocatalytic reaction is evaluated based on the pseudo-first-order model.

## Experimental procedure

### Materials and reagents

Ammonium hydroxide (25 %), ethanol (99.9 %), sulfuric acid (98 %), hydrochloric acid (37 %), and hydrogen peroxide (30 %) were purchased from Merck, Germany, and used without any purification. Potassium permanganate (98 %) was purchased from Alfa Aesar, USA, and the graphite flakes (94–97 %) was supplied by Timcal, Canada. The Zn foils were prepared by cold rolling of the Zn ingots (99.995 %, Calcimin, Iran) followed by annealing at 170 °C for 2 h. Samples with dimensions of  $40 \times 30 \times 0.2 \text{ mm}^3$  were cut and ground with emery papers.

## Oriented growth of ZnO nanorods on Zn substrate

The Zn substrates were first seeded by oxidization at 300 °C for 1 h in air and then were immersed in aqueous ammonia solutions with pH value of 10.75 in a Teflon-lined autoclave. The hydrothermal reaction was conducted at 130 °C for 9 h and then the autoclave was slowly cooled down to room temperature. The foils were removed from the solution, rinsed with distilled water, and then dried with hot air stream.

## Preparation of GO suspension

The graphene oxide was prepared by a modified Hummers method [40]. Firstly, 1 g graphite was added to 50 ml sulfuric acid and the suspension was cooled down to 0 °C in an ice-water bath. Three grams of potassium permanganate was then gradually added to the mixture, maintaining the temperature under 5 °C. The stirring continued for 3 h and the oxidation reaction was ceased by addition of 250 ml distilled water. The remaining insoluble manganese ions were reduced by addition of 5 ml hydrogen peroxide. The products were washed firstly with 1 M hydrochloric acid and then with distilled water to neutral pH. The graphite oxide was exfoliated in distilled water by means of ultrasonic treatment and was further centrifuged to remove un-oxidized or un-exfoliated graphite particles. After drying the supernatant, a 0.01 g l<sup>-1</sup> dispersion of GO in ethanol was prepared by sonication and the suspension was subsequently centrifuged at 8000 rpm to remove the undispersed particles.

## Synthesis of rGO–ZnO composite

The hydrothermally grown ZnO on Zn foils were put at the bottom of a sealed glass vessel and the GO suspension was added to a height of ~1.5 cm above the foils. The suspension was deoxygenated by a stream of Ar gas for 10 min. By illumination of a 30-W Hg lamp (254 nm, Philips, The Netherlands) for 30 min, the ZnO nanorods were excited to reduce the GO. Finally, the foils were removed from the suspension and then were dried at room temperature. These conditions were optimized to obtain the minimum thickness of the rGO layer since thicker layers will significantly reduce the intensity of the incident light (for exciting ZnO). It is noteworthy that thinner layers were also produced by decreasing the deposition time, but they lost their uniformity after evaporation of the solvent, leaving separate island-like regions.

## Photocatalytic test

ZnO nanorods grown on Zn foils with and without rGO with a total surface area of 60 cm<sup>2</sup> were placed at the bottom of a cuboid container; 45 ml of acid orange 7 with an initial concentration of 10 mg l<sup>-1</sup> was added to the container. To agitate the solution, Ar gas was blown from several points. A 30-W Hg lamp (254 nm) was used for the excitation of photocatalysts. Prior to the irradiation, the suspension was

agitated in dark for 30 min to determine the share of surface adsorption from the decolorization. A 3-ml sample was taken each 30 min during the experiment for UV–Vis spectroscopy test and the sample was returned to the reaction vessel after testing. The photocatalytic reaction was continued to 270 min. To evaluate the reusability of the composites, the photocatalytic test was repeated three times. After each test, the samples were washed with hydrogen peroxide and distilled water.

## Instrumentation

The scanning electron microscopy (SEM) images were taken by a field emission scanning electron microscope (Supra 35VP, Leo, Germany). The X-ray diffraction (XRD) patterns were recorded with a Bruker AXS advance powder diffractometer (USA) equipped with a Siemens X-ray gun, using Cu-K $\alpha$  radiation ( $\lambda = 1.5406 \text{ \AA}$ ). Room-temperature photoluminescence (PL) spectroscopy was carried out with a Perkin-Elmer luminescence spectrometer (LS 55, USA) with an excitation wavelength of 365 nm. A Shimadzu UV–visible spectrophotometer (UV-2550, Japan) was used to measure the UV–Vis absorption spectra. Raman spectroscopy measurements were taken using a Renishaw Raman microscopy system (InVia Reflex, UK) with a 532-nm laser. The X-ray photoelectron (XPS) spectra were recorded using a Thermo scientific XPS spectrometer (K-Alpha, UK) with a monochromatic Al K $\alpha$  radiation source (1486.8 eV). Spectral Data Processor (SDP, V. 4.1) software was employed for curve fittings and atomic percent calculations of XPS spectra. For photocatalytic studies, the concentration of the dye was measured using a Perkin-Elmer UV/Vis spectrophotometer (550 SE, USA) at  $\lambda_{\text{max}}$  of 485 nm. The decolorization efficiency was calculated using Eq. (1):

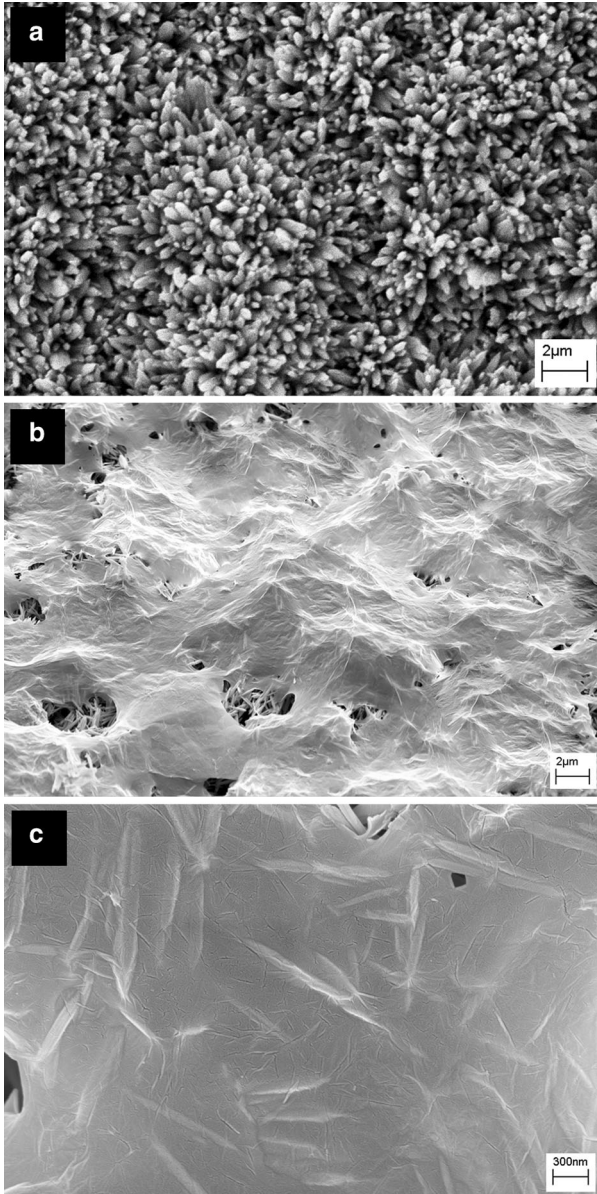
$$\text{Degradation (\%)} = [1 - (C/C_0)] \times 100 \quad (1)$$

where  $C_0$  and  $C$  are the initial and final concentrations of the dye, respectively.

## Results and discussion

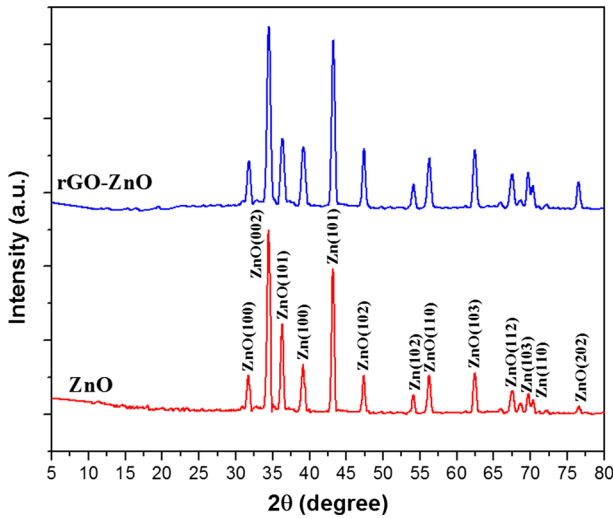
### Characteristics of rGO–ZnO composite

Figure 1 shows FE-SEM images of ZnO and rGO–ZnO on the Zn substrates. The growth of well-aligned and dense ZnO nanoarrays with an average diameter and length of  $\sim 150 \text{ nm}$  and  $\sim 2.5 \text{ \mu m}$ , respectively, via hydrothermal method is visible in Fig. 1a. The curled and corrugated rGO nanosheets with an average thickness of  $\sim 7 \text{ nm}$  are covered the entire surface of ZnO nanorods, which displays an efficient hybridization of rGO to ZnO (Fig. 1b). An observation of the surface morphology at a high magnification (Fig. 1c) reveals that the number of rGO layers is so few that the ZnO nanorods are still visible. The stretching of rGO nanosheets on the tips of the ZnO nanorods guarantees a suitable electrical connection between the composite components that can considerably enhance the photocatalytic performance.



**Fig. 1** FE-SEM images of: **a** ZnO nanorods and rGO-ZnO nanorod composites at **b** low and **c** high magnifications on Zn foils

The XRD patterns of the ZnO and rGO-ZnO are presented in Fig. 2. The diffraction peaks of nanorods are in accordance with JCPDS no. 36-1451 of ZnO [41], which confirms a hexagonal wurtzite lattice for hydrothermally grown nanoarrays. Reflections of Zn related to the substrate are also observable. The



**Fig. 2** XRD patterns of ZnO and rGO–ZnO

relative intensity of the (002) reflection of ZnO surpasses others, which indicates the orientation of nanorods along the C-axis. The relative texture coefficient of (002) over (100) diffraction peaks ( $TC_{002/100}$ ) is used to evaluate the orientation of the nanoarrays, which can be expressed as Eq. (2) [42]:

$$TC_{002/100} = \frac{(I_{002}/I_{002}^0)}{\left[ (I_{100}/I_{100}^0) + (I_{002}/I_{002}^0) \right]} \tag{2}$$

where  $I_{002}$  and  $I_{100}$  are the diffraction intensities of (002) and (100) planes, respectively and  $I^0$  is the diffraction intensity of the randomly oriented powder sample given by JCPDS no. 36-1451. Texture coefficients of about 0.5 refer to randomly oriented structures while values close to 1 refer to highly oriented structures [42]. The texture coefficient for the synthesized ZnO was obtained 0.85 revealing a good alignment of ZnO nanorods. The XRD pattern of rGO–ZnO composite is similar to pure ZnO nanorods and the usual reflections belonging to rGO are not detectable because the intensities of the sharp ZnO and Zn peaks are incomparably higher than the small semi-amorphous hill-like peak of the rGO appeared at  $\sim 25^\circ$ . Furthermore, by utilization of the Debye–Scherrer’s equation (Eq. 3), the crystallite size of the ZnO was calculated (based on 002 peak) to be  $\sim 19.2$  nm [43]:

$$D = \frac{0.9 \lambda}{\beta \text{Cos}\theta} \tag{3}$$

where  $D$  is the average crystallite size ( $\text{\AA}$ ),  $\lambda$  is the wavelength of the X-ray (Cu  $K_\alpha = 1.5406 \text{\AA}$ ),  $\beta$  is the full width at half maximum (FWHM) intensity of the peak (rad) and  $\theta$  is the diffraction angle.

Due to the exceptional electrical conductance of graphene, an efficient transfer of charge carriers and thus a longer lifetime of photogenerated electron–hole pairs are expected [44]. The effective charge transfer from ZnO nanorods to rGO nanosheets and the prolonged recombination of electron–hole pairs were clearly shown by means of room temperature PL spectroscopy (Fig. 3). The UV emission appeared at  $\sim 377$  nm and the visible emission which is a broad peak between 450 and 750 nm with a maximum located at  $\sim 575$  nm (arising from the oxygen vacancies of its lattice [45]) are extremely quenched by incorporation of rGO nanosheets to ZnO nanorods. The UV-assisted reduction of GO restores  $sp^2$  hybridization of the carbon atoms in rGO, which enables it to transfer photoexcited electrons of ZnO nanorods. The highly mobile  $\pi$ -orbital electrons of rGO provide a convenient extra path for charge carriers and prevent from direct recombination of electron–hole pairs, which subsequently increase their lifespan.

UV–Vis spectroscopy is an informative and important technique to determine the change in the absorption of a photocatalyst. Figure 4a displays the UV–Vis absorption spectra of ZnO nanoarrays and rGO–ZnO nanocomposite. According to the spectra, ZnO presents its characteristic absorption sharp edge rising from 400 nm, while the rGO–ZnO composite shows a more intense background absorption in the visible light region and its characteristic absorption sharp edge experiences a small red shift. The band gap ( $E_g$ ) was measured from the absorbance spectra using the following relationships [46]:

$$\alpha d = \ln\left(\frac{1}{T}\right) \quad (4)$$

$$(\alpha h\nu) = A(h\nu - E_g)^P \quad (5)$$

where  $\alpha$  is the absorption coefficient,  $d$  is the thickness of the film,  $T$  is the transmittance,  $A$  is a constant, and  $h\nu$  is the photon energy.  $P$  is a constant that depends

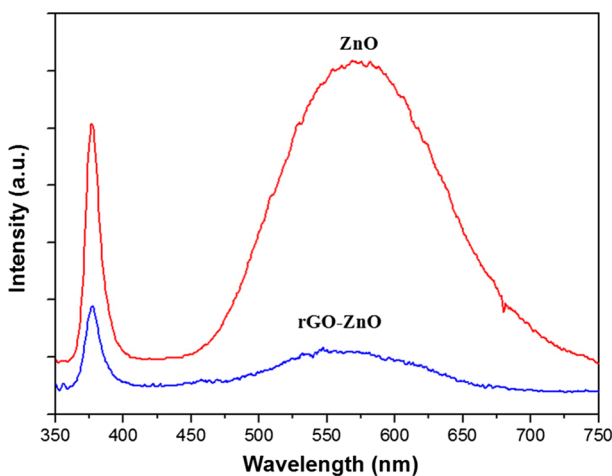


**Fig. 3** PL spectra of ZnO and rGO–ZnO



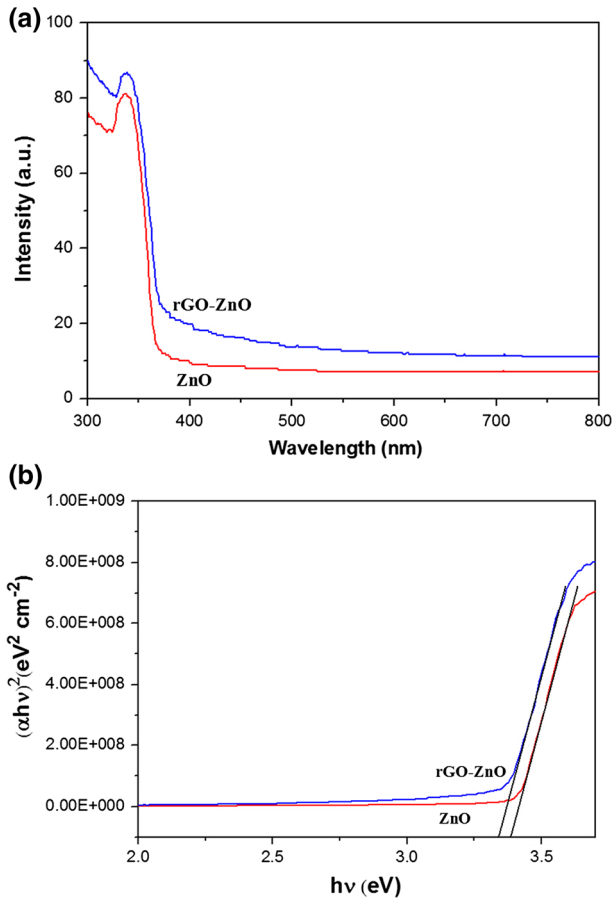


**Fig. 4** **a** Absorbance spectra of ZnO and rGO–ZnO and **b** calculation of direct band gap by using Tauc's plot

on the type of the electronic transitions so that  $P$  is equal to 0.5 for allowed direct transition. However,  $P$  may also be equal to 1.5 for forbidden direct transition, 2 for indirect allowed transition, and 3 for indirect forbidden transition [47]. Regarding that ZnO is a direct band gap semiconductor, the optical band gap was obtained by plotting  $(\alpha h\nu)^2$  as a function of photon energy ( $h\nu$ ), as shown in Fig. 4b. The intercepts of the extrapolation to zero absorption with photon energy axis give the values of the direct energy gap. The results indicated that the band gap energy of ZnO after incorporation of rGO was decreased from  $\sim 3.41$  to  $\sim 3.35$  eV, mainly due to the transfer of the photogenerated electron from ZnO to rGO.

The successful UV-assisted reduction of GO to rGO was further confirmed by Raman spectroscopy and X-ray photoelectron spectroscopy techniques. The Raman spectra of ZnO, GO and rGO–ZnO are illustrated in Fig. 5. Three dominant peaks are detectable at  $329$ ,  $440$ , and  $584$   $\text{cm}^{-1}$  in the ZnO Raman spectrum. The

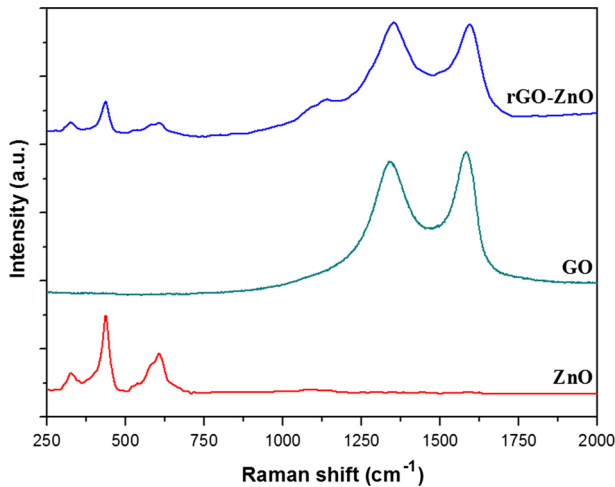


**Fig. 5** Raman spectra of GO, ZnO, and rGO-ZnO

$329\text{ cm}^{-1}$  peak is generated from second-order Raman spectrum arising from zone-boundary phonons of hexagonal ZnO. The intense peak that appeared at  $440\text{ cm}^{-1}$  is assigned to non-polar optical phonon  $E_2$  (HI) vibration mode of ZnO in wurtzite structure. Finally, the peak at  $584\text{ cm}^{-1}$  corresponds to the  $E_1$  (LO) mode of hexagonal ZnO, which is associated with the oxygen deficiencies [48]. On the other hand, the Raman spectrum of GO is dominated by two characteristic peaks of carbonaceous materials located at  $\sim 1346$  and  $\sim 1589\text{ cm}^{-1}$ , namely D and G bands. D band arises from the defects created by the attachment of oxygen-containing functional groups (OFGs) on the graphene's basal plane and G band assigns to the first-order scattering of the  $E_{2g}$  mode [49]. The Raman spectrum of rGO-ZnO composite showed similar characteristic peaks of ZnO as well as G and D bands of GO. Furthermore, the G peak in rGO-ZnO is slightly blue-shifted by  $5\text{ cm}^{-1}$  compared to GO, suggesting the reduction of GO to rGO. The intensity ratios of the D and G bands ( $I_D/I_G$ ) in GO and rGO-ZnO were determined 0.94 and 1.01, respectively. It is known that GO is a highly defective structure in which  $I_D/I_G$  decreases as an increasing defect density results in a more amorphous carbon structure, attenuating the Raman peaks [50]. Thus, the increased intensity ratio of the D and G bands in the rGO-ZnO composite reveals a decrease in the amount of defects induced by the attachment of OFGs upon UV-assisted reduction of GO [51].

XPS survey spectrum (Fig. 6a) demonstrates that the rGO-ZnO composite mostly contains Zn, O, and C. In spite of the fact that the detection depth of XPS technique does not exceed 6 nm [52], the rGO layers are so thin that strong peaks of Zn are clearly detectable in the survey spectrum. In order to evaluate the effectiveness of photocatalytic reduction in the elimination of OFGs, the carbon-to-oxygen atomic ratio (C/O) was calculated. The  $C/O \approx 5.2$  for rGO-ZnO composite is comparable with the majority of conventional reduction processes of GO [53], even though the reduction time is shorter than most of them and a fraction of oxygen

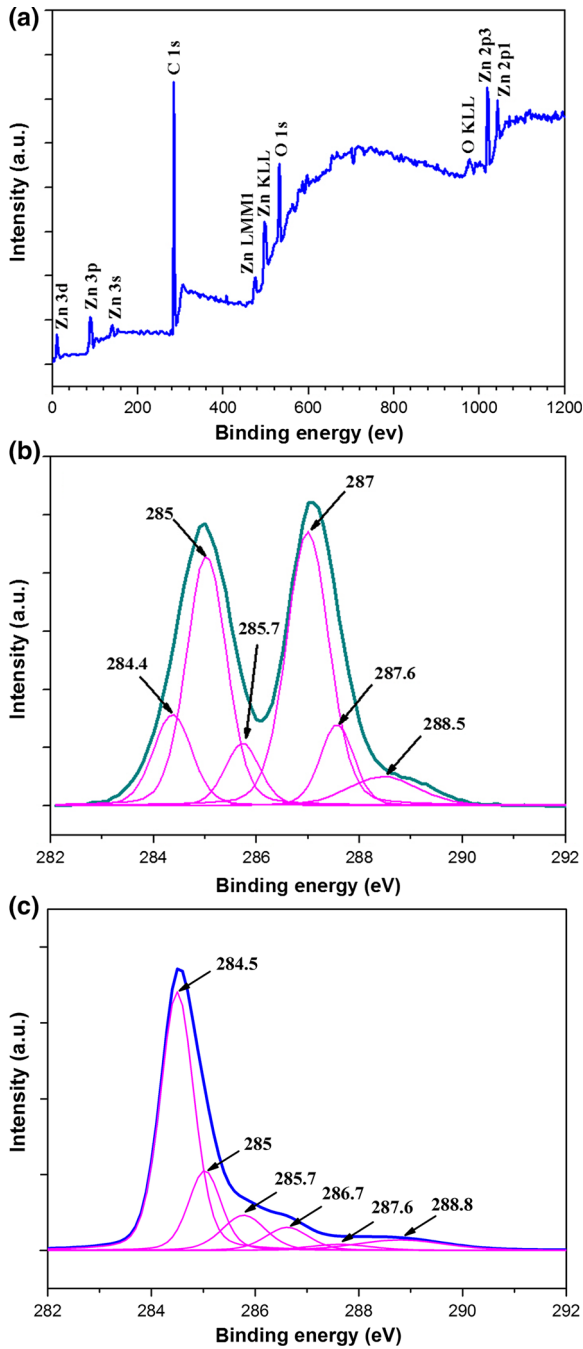
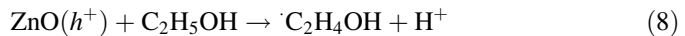
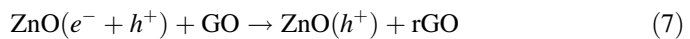
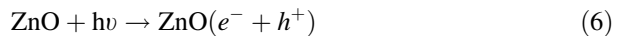


**Fig. 6** a XPS survey spectrum of rGO–ZnO composite, deconvoluted high-resolution C1 s spectra of b GO and c rGO–ZnO

atoms belongs to ZnO. The electrical conductance of graphene is a critical parameter for enhancement of the photocatalytic activity of rGO–ZnO composites. However, the formation of covalent bonds between OFGs and carbon atoms drastically reduces the conductivity of graphene. To monitor the changes in these functional groups upon UV-assisted reduction, the high-resolution C 1s XPS spectra for GO and rGO–ZnO were deconvoluted as shown in Fig. 6b and c. Two main components located at 284.5 and 285 eV are assigned to the  $sp^2$  and  $sp^3$  hybridizations of carbon atoms, respectively. Besides, the major peak at  $\sim 287$  eV is consisted of four functional groups: (1) hydroxyl (C–OH, 285.7 eV), (2) epoxide (C–O–C, 287 eV), (3) carbonyl ( $>C=O$ , 287.6 eV), and (4) carboxyl (O=C–OH, 288.5 eV) [54, 55]. The  $sp^3$  hybridization of carbon atoms and the chemical shifts of the core level to higher binding energies are attributed to the attachment of more electronegative OFGs. To discover the change in the amount of OFGs during photocatalytic reduction, the percentage areas for different OFGs were determined from deconvoluted XPS spectra (Table 1). A significant reduction in the amount of OFGs occurred after UV-assisted reduction so that the concentration of epoxide and carbonyl bonds reduced approximately 82 and 69 %, respectively.

Consequently, the reduction of GO and subsequent attachment of rGO to ZnO nanorods occurs simultaneously through the transfer of photogenerated electrons from ZnO to GO while the remaining holes are consumed by ethanol as a hole-scavenger agent [35]. The major reaction steps in the UV-assisted reduction mechanism for synthesis of rGO–ZnO composite are summarized in Eqs. (6–8):



### Photocatalytic behavior of rGO–ZnO composite

The effect of hybridization of ZnO with rGO on the photocatalytic activity was investigated through the decolorization of AO7 under UV-C illumination (Fig. 7a). The concentration changes of the dye molecules prior to the light irradiation (Fig. 7b) indicate that rGO–ZnO exhibits higher adsorption compared to ZnO. The results of photocatalytic degradation of AO7 were analyzed by a pseudo-first-order kinetic model, which can be expressed as [56]:

**Table 1** Percentage areas of the oxygen containing bonds obtained from XPS deconvolution analysis

	C–C ( $sp^2$ )	C–C ( $sp^3$ )	C–OH	C–O–C	$>C=O$	O=C–OH
GO	11	31	6.8	36.3	8.5	6.4
rGO–ZnO	57.5	17.1	10.1	6.6	2.6	6.2

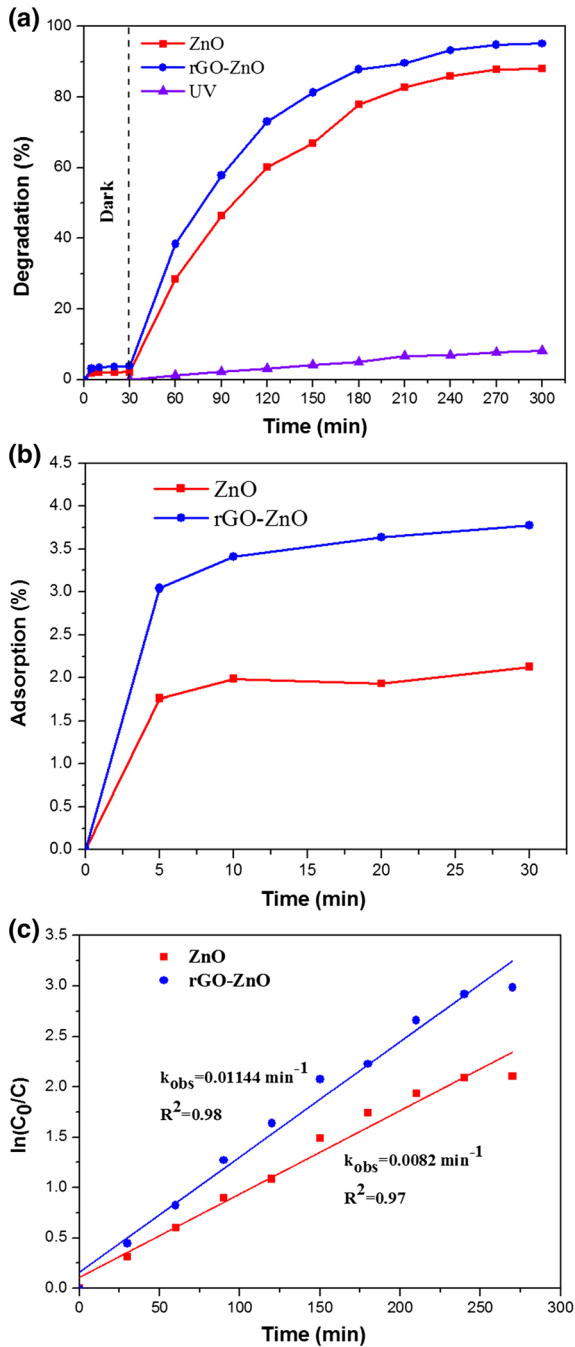
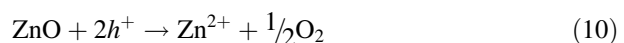


**Fig. 7** **a** Photocatalytic degradation of AO7 by means of ZnO and rGO–ZnO under UV-C illumination. **b** Surface adsorption of the dye prior to UV illumination. **c** Derivation of the pseudo-first-order model's rate constant by a linear regression

$$\frac{dC}{dt} = -k_{\text{obs}}C \quad (9)$$

where  $t$  is the reaction time and  $k_{\text{obs}}$  is the pseudo-first-order kinetic model's rate constant.  $k_{\text{obs}}$  was obtained by the application of a least square regression analysis, as shown in Fig. 7c. The AO7 removal rate increases  $\sim 40\%$  after incorporation of rGO to ZnO nanorods. The enhancement of the photocatalytic efficiency and rate in rGO–ZnO composite is mostly ascribed to the very efficient adsorption of dye molecules and the reduction of electron–hole pair recombination. The rGO with a high surface area anchors organic molecules by means of its  $\pi$ -orbital electrons [57]. On the other hand, the photocatalytic performance was influenced by the band gap changes of ZnO induced by rGO (Fig. 4). Considering the relative band position of ZnO (conduction band of  $-4.05$  eV and valence band of  $-7.25$  eV vs. vacuum) and rGO ( $-4.42$  eV) [47], photogenerated electrons can simply transfer from ZnO conduction band to rGO. The electrons are preserved on the rGO and then migrate to degrade AO7 molecules. Nevertheless, the compositing of ZnO with rGO leads to the attenuation of the incident light. It has been shown that graphene absorbs  $\sim 2.3\%$  of the visible light while this absorption quickly amplifies to  $\sim 10\%$  in ultraviolet [58]. Furthermore, by increasing of the size and the number of graphene layers and by attachment of the functional groups to graphene (as in rGO), the absorption coefficient increases [59]. Thus, careful care should be considered during the compositing of rGO with ZnO to avoid from the formation of a thick rGO layer on ZnO nanorods.

It is noteworthy that the difference in the photocatalytic activity of rGO–ZnO and ZnO increases by progression of the photocatalytic reaction, as shown in Fig. 7a. The recycled photocatalytic experiments for the decolorization of AO7 are conducted to assess the photostability of the catalyst and the results are illustrated in Fig. 8. Although 88% of AO7 was degraded after 270 min when ZnO was used for the first time, its photocatalytic performance was significantly decreased after three recycles so that only 17% of the dye was degraded (Fig. 8a). Considering the share of photolysis in degradation of dye molecules, the photocatalytic activity of ZnO in the 2nd and 3rd time reuses is virtually negligible, which can be ascribed to the intense photocorrosion of ZnO. The photoinduced dissolution of ZnO consists of the reaction of unsaturated surface oxygen atoms with photogenerated holes trapped on the surface through a series of consecutive reactions [14, 60], which can be represented as the following overall equation:



The compositing of ZnO nanorods by rGO leads to a significant enhancement of the photostability, which allows it to be used for longer periods of time, as shown in Fig. 8b. The recycled usage of rGO–ZnO composite for 2nd and 3rd times could degrade 89 and 74% of AO7 after 270 min. Thus, the photocorrosion of the ZnO is considerably hindered by rGO, as illustrated in Fig. 8c. Although there is a general agreement on the photocorrosion mechanism of ZnO, yet there is a considerable vagueness on the protective effect of the incorporation of carbonaceous materials

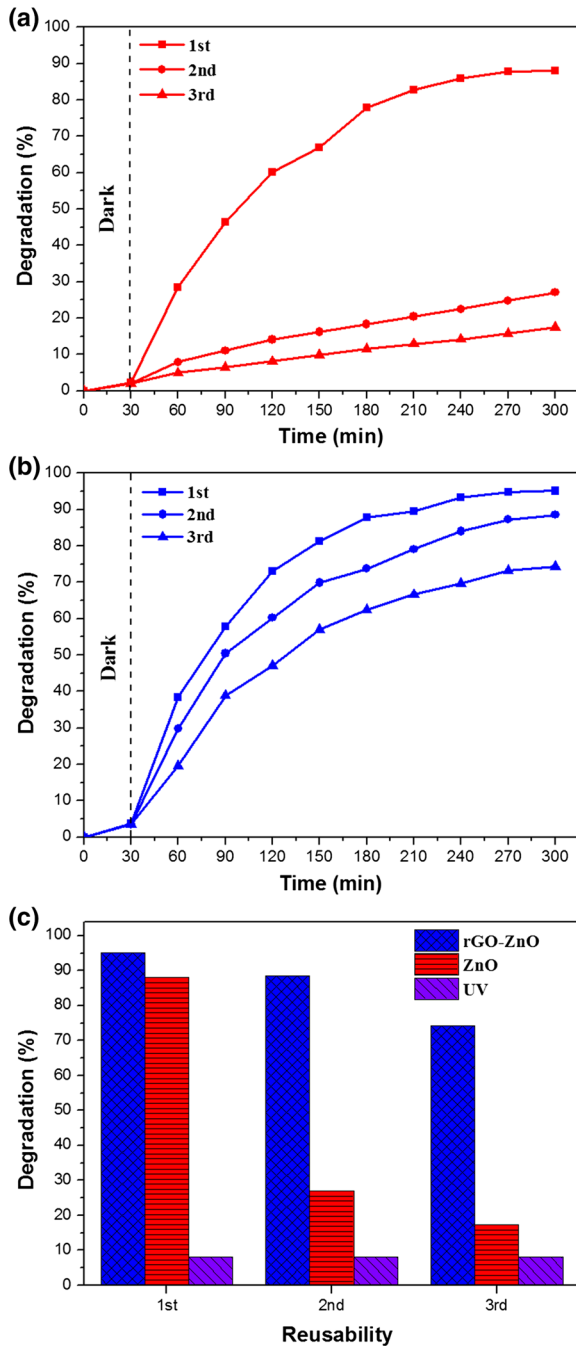


**Fig. 8** Recycled photocatalytic activity of: **a** ZnO and **b** rGO-ZnO. **c** Comparison of the reusability of rGO-ZnO and ZnO

(e.g., fullerene, carbon nanotube, and graphene). The bond formation between unsaturated surface oxygen atoms of ZnO and carbon atoms of carbonaceous nanostructure has been proposed as the dominant protection mechanism [5, 14, 61]. However, at least as in this case, the direct contact between rGO and ZnO for the formation of such bonds is so limited that this mechanism cannot be the responsible for the photostability. Instead, the facilitation of the hole-consumer photocatalytic reaction through the incorporation of rGO would be the principle mechanism. As previously discussed, the  $\pi$ -orbital electrons of the rGO can adsorb and anchor the organic molecules, which results in an effective interaction between the photocatalyst and the dye. In fact, graphene assists the dye degradation reaction without experiencing a notable change. Thus, the dye molecules act as hole scavengers in the photodegradation of AO7, which inhibits the photoinduced dissolution of ZnO (Eq. 10) and enhancing the photostability.

## Conclusions

rGO–ZnO sandwich-like composite was successfully synthesized via in situ hybridization of immobilized ZnO nanorods and rGO through photocatalytic reduction of GO. The reduction of GO and incorporation of rGO nanosheets to ZnO nanorods were validated via XRD, SEM, Raman spectroscopy, and XPS techniques while the efficient electrical connectivity of rGO and ZnO and reduction of photoelectron–hole pair recombination were confirmed by PL spectroscopy. rGO–ZnO catalyst exhibited a superior photocatalytic performance than ZnO, which can be attributed to the prolonged lifespan of electron–hole pairs and effective adsorption of dye molecules. The incorporation of rGO to ZnO resulted in a better photostability, which was ascribed to the better supplementation of dye molecules to scavenge the photogenerated holes. The proposed method is employable for fabrication of similar architectures (sandwich-like) of graphene/immobilized semiconductor for numerous applications such as solar cells, gas sensors, and photocatalysts.

**Acknowledgments** The authors thank the University of Tabriz (Iran) for all of the support provided.

## References

1. P. Ju, H. Fan, S. Ai, D. Zhang, Y. Wang, *Res. Chem. Intermed.* **41**, 3683 (2015)
2. A.R. Khataee, A. Karimi, R.D.C. Soltani, M. Safarpour, Y. Hanifehpour, S.W. Joo, *Appl. Catal. A-Gen.* **488**, 160 (2014)
3. N. Daneshvar, D. Salari, A.R. Khataee, *J. Photochem. Photobiol. A.* **162**, 317 (2004)
4. K. Dai, G. Dawson, S. Yang, Z. Chen, L. Lu, *Chem. Eng. J.* **191**, 571 (2012)
5. H. Fu, T. Xu, S. Zhu, Y. Zhu, *Environ. Sci. Technol.* **42**, 8064 (2008)
6. T. Lv, L. Pan, X. Liu, T. Lu, G. Zhu, Z. Sun, *J. Alloys Compd.* **509**, 10086 (2011)
7. S. Abdolhosseinzadeh, H. Asgharzadeh, H.S. Kim, *Sci. Rep.* **5**, 10160 (2015)
8. G. Xie, K. Zhang, B. Guo, Q. Liu, L. Fang, J.R. Gong, *Adv. Mater.* **25**, 3820 (2013)
9. G. Xie, K. Zhang, H. Fang, B. Guo, R. Wang, H. Yan, L. Fang, J.R. Gong, *Chem. Asian J.* **8**, 2395 (2013)
10. H. Fan, X. Zhao, J. Yang, X. Shan, L. Yang, Y. Zhang, X. Li, M. Gao, *Catal. Commun.* **29**, 29 (2012)



11. Q. Li, B. Guo, J. Yu, J. Ran, B. Zhang, H. Yan, J.R. Gong, *J. Am. Chem. Soc.* **133**, 10878 (2011)
12. J. Zhang, J. Yu, M. Jaroniec, J.R. Gong, *Nano Lett.* **12**, 4584 (2012)
13. R.C. Pawar, D. Cho, C.S. Lee, *Curr. Appl. Phys.* **13**, 50 (2013)
14. L. Zhang, H. Cheng, R. Zong, Y. Zhu, *J. Phys. Chem. C* **113**, 2368 (2009)
15. R.C. Pawar, C.S. Lee, *Appl. Catal. B Environ.* **144**, 57 (2014)
16. A. Olad, R. Nosrati, *Res. Chem. Intermed.* **38**, 323 (2012)
17. R.C. Pawar, D.H. Choi, J.S. Lee, C.S. Lee, *Mat. Chem. Phys.* **151**, 167 (2015)
18. A. Phuruangrat, S. Mad-ahin, O. Yayapao, S. Thongtem, T. Thongtem, *Res. Chem. Intermed.* (2015). doi:10.1007/s11164-015-1963-z
19. L. Xu, Y.L. Hu, C. Pelligra, C.H. Chen, L. Jin, H. Huang, S. Sithambaram, M. Aindow, R. Joesten, S.L. Suib, *Chem. Mater.* **21**, 2875 (2009)
20. J. Xie, Y. Li, W. Zhao, L. Bian, Y. Wei, *Powder Technol.* **207**, 140 (2011)
21. C. Zou, F. Liang, S. Xue, *Res. Chem. Intermed.* (2014). doi:10.1007/s11164-014-1620-y
22. J.L. Yang, S.J. An, W.I. Park, G.C. Yi, W. Choi, *Adv. Mater.* **16**, 1661 (2004)
23. S. Abdolhosseinzadeh, H. Asgharzadeh, *Adv. Mater. Res.* **829**, 421 (2014)
24. A.K. Singh, G.S. Thool, S.R. Deo, R.S. Singh, A. Gupta, *Res. Chem. Intermed.* **38**, 2041 (2012)
25. M.H. Wong, A. Berenov, X. Qi, M.J. Kappers, Z.H. Barber, B. Illy, Z. Lockman, M.P. Ryan, J.L. MacManus-Driscoll, *Nanotechnology* **14**, 968 (2003)
26. S. Ma, R. Li, C. Lv, W. Xu, X. Gou, *J. Hazard. Mater.* **192**, 730 (2011)
27. T. Xu, L. Zhang, H. Cheng, Y. Zhu, *Appl. Catal. B Environ.* **101**, 382 (2011)
28. X. Liu, L. Pan, Q. Zhao, T. Lv, G. Zhu, T. Chen, T. Lu, Z. Sun, C. Sun, *Chem. Eng. J.* **183**, 238 (2012)
29. S. Darbari, V. Ahmadi, P. Afzali, Y. Abdi, M. Fedaa, *J. Nanopart. Res.* **16**, 1 (2014)
30. M.K. Kavitha, H. John, P. Gopinath, R. Philip, *J. Mater. Chem. C* **1**, 3669 (2013)
31. R. Lv, X. Wang, W. Lv, Y. Xu, Y. Ge, H. He, G. Li, X. Wu, X. Li, Q. Li, *J. Chem. Technol. Biot.* **90**, 550 (2014)
32. Y. Kaikun, X. Congkang, H. Liwei, Z. Lianfeng, W. Howard, *Nanotechnology* **22**, 405401 (2011)
33. U. Alver, W. Zhou, A.B. Belay, R. Krueger, K.O. Davis, N.S. Hickman, *Appl. Surf. Sci.* **258**, 3109 (2012)
34. H.N. Tien, V.H. Luan, L.T. Hoa, N.T. Khoa, S.H. Hahn, J.S. Chung, E.W. Shin, S.H. Hur, *Chem. Eng. J.* **229**, 126 (2013)
35. G. Williams, P.V. Kamat, *Langmuir* **25**, 13869 (2009)
36. O. Akhavan, *Carbon* **49**, 11 (2011)
37. M. Bideau, B. Claudel, C. Dubien, L. Faure, H. Kazouan, *J. Photochem. Photobiol. A* **91**, 137 (1995)
38. M. Fathinia, A. Khataee, *Appl. Catal. A Gen.* **491**, 136 (2015)
39. S. Baruah, J. Dutta, *Sci. Technol. Adv. Mater.* **10**, 013001 (2009)
40. O. Akhavan, *Carbon* **48**, 509 (2010)
41. Joint Committee on Powder Diffraction, Powder Diffraction File, Card 36–1451(ZnO), (ICDD, Swarthmore, PA, 1996)
42. J. Lu, Z. Ye, J. Huang, L. Wang, B. Zhao, *Appl. Surf. Sci.* **207**, 295 (2003)
43. A.L. Patterson, *Phys. Rev.* **56**, 978 (1939)
44. Z. Chen, N. Zhang, Y.-J. Xu, *Cryst. Eng. Commun.* **15**, 3022 (2013)
45. K. Pita, P. Baudin, Q. Vu, R. Aad, C. Couteau, G. Léronnel, *Nanoscale Res. Lett.* **8**, 1 (2013)
46. H.A. Wahab, A.A. Salama, A.A. El-Saeid, O. Nur, M. Willander, I.K. Battisha, *Res. Phys.* **3**, 46 (2013)
47. X. Liu, L. Pan, T. Lv, T. Lu, G. Zhu, Z. Sun, C. Sun, *Catal. Sci. Technol.* **1**, 1189 (2011)
48. J.Y. Li, H. Li, *Nanoscale Res. Lett.* **4**, 165 (2009)
49. D. Yang, A. Velamakanni, G. Bozkoku, S. Park, M. Stoller, R.D. Piner, S. Stankovich, I. Jung, D.A. Field, C.A. Ventrice Jr, R.S. Ruoff, *Carbon* **47**, 145 (2009)
50. M.M. Lucchese, F. Stavale, E.H.M. Ferreira, C. Vilani, M.V.O. Moutinho, R.B. Capaz, C.A. Achete, A. Jorio, *Carbon* **48**, 1592 (2010)
51. K. Zhou, Y. Zhu, X. Yang, X. Jiang, C. Li, *New J. Chem.* **35**, 353 (2011)
52. C.D. Wagner, W.M. Riggs, L.E. Davis, J.F. Moulder, *Handbook of X-Ray Photoelectron Spectroscopy* (Perkin-Elmer Corporation, Physical Electronics, Eden Prairie, 1979)
53. C.K. Chua, M. Pumera, *Chem. Soc. Rev.* **43**, 291 (2014)
54. S. Yumitori, *J. Mater. Sci.* **35**, 139 (2000)
55. A. Ganguly, S. Sharma, P. Papakonstantinou, J. Hamilton, *J. Mater. Chem. C* **115**, 17009 (2011)
56. N. Daneshvar, M.H. Rasoulifard, A.R. Khataee, F. Hosseinzadeh, *J. Hazard. Mater.* **143**, 95 (2007)

57. T. Kuila, S. Bose, A.K. Mishra, P. Khanra, N.H. Kim, J.H. Lee, *Prog. Mater. Sci.* **57**, 1061 (2012)
58. V.G. Kravets, A.N. Grigorenko, R.R. Nair, P. Blake, S. Anissimova, K.S. Novoselov, A.K. Geim, *Phys. Rev. B.* **81**, 155413 (2010)
59. R. Su, S.F. Lin, D.Q. Chen, G.H. Chen, *J. Mater. Chem. C.* **118**, 12520 (2014)
60. A.L. Rudd, C.B. Breslin, *Electrochim. Acta* **45**, 1571 (2000)
61. C. Han, M.-Q. Yang, B. Weng, Y.-J. Xu, *Phys. Chem. Chem. Phys.* **16**, 16891 (2014)